

# Molecular mechanism of substrate recognition by folate transporter SLC19A1

## Authors:

Yu Dang<sup>1</sup>, Dong Zhou<sup>2</sup>, Xiaojuan Du<sup>3†</sup>, Hongtu Zhao<sup>4</sup>, Chia-Hsueh Lee<sup>4</sup>, Jing Yang<sup>3</sup>,  
Changdong Qin<sup>5</sup>, Zhenxi Guo<sup>5</sup>, and Zhe Zhang<sup>1,2,3\*</sup>

## Affiliations:

<sup>1</sup>State Key Laboratory of Membrane Biology, Peking University-Tsinghua University-National Institute of Biological Sciences Joint Graduate Program, Academy for Advanced Interdisciplinary Studies, Peking University, Beijing 100871, China

<sup>2</sup>Center for Life Sciences, Academy for Advanced Interdisciplinary Studies, Peking University, Beijing 100871, China

<sup>3</sup>School of Life Sciences, Peking University, Beijing 100871, China

<sup>4</sup>Department of Structural Biology, St. Jude Children's Research Hospital, Memphis, TN 38105, United States

<sup>5</sup>Cryo-EM Platform, School of Life Sciences, Peking University, Beijing 100871, China

†Present address: Peking University First Hospital, Peking University Health Science Center, Beijing 100191, China

\*Correspondence should be addressed to [zzhang01@pku.edu.cn](mailto:zzhang01@pku.edu.cn).

## Abstract

Folate (vitamin B<sub>9</sub>) is the coenzyme involved in one-carbon transfer biochemical reactions essential for cell survival and proliferation, with its inadequacy causing developmental defects or severe diseases. Notably, mammalian cells lack the ability to *de novo* synthesize folate but instead rely on its intake from extracellular sources via specific transporters or receptors, among which SLC19A1 is the ubiquitously expressed one in tissues. However, the mechanism of substrate recognition by SLC19A1 has been unclear. Here we report the cryo-EM structures of human SLC19A1 and its complex with 5-methyltetrahydrofolate at 3.5-3.6 Å resolution and elucidate the critical residues for substrate recognition. In particular, we reveal that two variant residues among SLC19 subfamily members would designate the specificity for folate. Moreover, we identify intracellular thiamine pyrophosphate as the favorite coupled substrate for folate transport by SLC19A1. Together, this work has established the molecular basis of substrate recognition by this central folate transporter.

## Introduction

Folate (vitamin B<sub>9</sub>) is the coenzyme serving as the single-carbon donor in many biochemical reactions, e.g., the synthesis of purine and thymidylate, the metabolism of serine and methionine, and the methylation of nucleic acids and proteins<sup>1</sup>. Given such essential roles in cell growth, proliferation, and differentiation, folate inadequacy would lead to severe developmental defects or neurological disorders in humans<sup>2,3</sup>.

Mammalian cells lack the ability to *de novo* synthesize folate and must obtain it from extracellular sources such as foods. Three different systems are known for the transmembrane uptake of folate in mammals, i.e., the proton-coupled folate transporter SLC46A1<sup>4</sup>, the folate receptors (FRs)<sup>5-7</sup>, and the reduced folate carrier SLC19A1<sup>8,9</sup>. SLC46A1 is predominantly expressed in the gastrointestinal tract and is responsible for dietary folate absorption. Accordingly, SLC46A1 exhibits an optimal activity at acidic pH and couples folate transport to proton influx<sup>10,11</sup>. On the other hand, FRs take folate into cells via receptor-mediated endocytosis, primarily for folate delivery to the brain or folate retention in the kidney<sup>7,12,13</sup>. Notably, both SLC46A1 and FRs exert tissue-specific roles in folate transport. In contrast, SLC19A1 is ubiquitously expressed in the body and represents the major system of folate transport in diverse cell types<sup>13</sup>. For instance, though all three systems could facilitate the cellular uptake of antifolate drugs for cancer chemotherapy, SLC19A1 is the predominant route in many cancer cells<sup>11,14,15</sup>. Indeed, decreased expression or loss-of-function mutations of SLC19A1 in cancers would result in resistance to antifolate treatments<sup>16</sup>. Additionally, while SLC46A1 and FRs have equal affinities to folate and its reduced derivatives (e.g., 5-methyltetrahydrofolate, 5-MTHF), SLC19A1 shows a strong preference for the reduced derivatives<sup>2</sup>.

The structural mechanisms of folate transport by SLC46A1 and FRs have been elucidated<sup>17-19</sup>. However, despite its central role in folate uptake among different tissues, the molecular basis of substrate recognition by SLC19A1 has remained unclear. Here we report the cryo-EM structures of human SLC19A1 and its complex with 5-MTHF at 3.5-3.6 Å resolution and demonstrate the critical residues for substrate binding. In particular, we reveal two variant residues among SLC19 subfamily members, i.e., Arg133 and Gln377 in SLC19A1 vs. Glu138 and Met401 in SLC19A2, or Glu120 and Met384 in SLC19A3, being sufficient to designate the specificity for folate. Moreover, we identify intracellular thiamine pyrophosphate (TPP) as the favorite coupled substrate for folate transport by SLC19A1. These results have established the key mechanism of substrate recognition by SLC19A1.

## Results

### Structures of human SLC19A1 and its complex with 5-MTHF

Human SLC19A1 has 591 residues with a molecular weight of 65 kDa and is mainly composed of 12 transmembrane helices (TMs). As a result, the majority of the protein would be embedded in detergent micelles without obvious features when extracted from the cell membrane, limiting the structural determination by cryo-EM. To overcome this issue, we exploited the BRIL/Fab/Nb module<sup>20-22</sup>, which helped provide the apparent shape for particle alignment. The N-terminal 23 residues preceding the TM1 of SLC19A1 were replaced by the BRIL domain (Fig. 1a). Importantly, wild-type SLC19A1 or BRIL-SLC19A1 overexpressed in HEK293F cells exhibited comparable transport activity for a standard substrate [<sup>3</sup>H]-radiolabeled methotrexate ([<sup>3</sup>H]-MTX)<sup>23</sup>, indicating that the BRIL-tag would not affect the normal function of SLC19A1 (Fig. 1b and Extended Data Fig. 1a).

We purified the BRIL-SLC19A1 protein and then added anti-BRIL Fab and anti-Fab nanobody (Nb) to assemble the BRIL-SLC19A1/Fab/Nb ternary complex (Fig. 1c). The cryo-EM map of the ternary complex was collected and successfully reconstructed to 3.6-Å resolution (Fig. 1d, and Extended Data Fig. 2 and Table 1). In the structure of BRIL-SLC19A1, the last helix of BRIL rotated around its joint region with the TM1 of SLC19A1, and as a result, the four-helical bundle of BRIL resided parallel to the cell membrane. In addition, BRIL leaned on the intracellular loop between TM4 and TM5 of SLC19A1 via the electrostatic interactions between three acidic residues of BRIL (Glu4, Asp5, and Glu8) and two basic residues (Arg145 and Arg148) of SLC19A1 (Fig. 1e), stabilizing the current conformation of BRIL-SLC19A1. SLC19A1 adopted the classical major facilitator superfamily (MFS) fold<sup>24,25</sup> with two discrete TM bundles (TM1-6 and TM7-12) (Fig. 1f, g), and all the TM regions were clearly resolved in the cryo-EM structure. SLC19A1 was present in the inward-facing conformation, i.e., the intracellular gate between TM4-5 and TM10-11 was open while the extracellular gate was closed by the regions of TM1, 2, and 7 (Fig. 1g). A notable feature was that a segment of TM1 (Ile41-Phe47) was unwound in the extracellular leaflet of the membrane (Fig. 1g). It has been documented that the discontinuity of transmembrane helices could play pivotal roles in transporters and ion channels by creating substrate-binding sites or providing flexible gating hinges<sup>26-30</sup>. On the other hand, the EM densities of the intracellular loop between TM6 and TM7 (residues 214-249) and the C-terminal cytoplasmic region (residues 452-591) of SLC19A1 were invisible (Fig. 1f, g), implicating their high motility and in line with their dispensable role for the transporter function<sup>11</sup>.

In parallel to the strategy of the BRIL module, we also identified one nanobody against SLC19A1 from a synthetic yeast-display library<sup>31</sup>. Using the nanobody-based legobody strategy<sup>32</sup>, we determined the cryo-EM structure of the SLC19A1/legobody complex to a medium resolution

(~5 Å). The nanobody bound the TM6-7 linker region of SLC19A1, and the overall structure of the nanobody-bound SLC19A1 was almost identical to that observed in BRIL-SLC19A1 (Extended Data Fig. 3a). Given its higher resolution, the structure of BRIL-SLC19A1 (hereafter referred to as SLC19A1) was pursued in our further studies.

We next determined the cryo-EM structure of SLC19A1 in complex with its preferred substrate 5-MTHF at 3.5-Å resolution (Fig. 2a, and Extended Data Fig. 4 and Table 1). Similar to the apo-structure of SLC19A1, the SLC19A1/5-MTHF complex was in the inward-facing conformation (Fig. 2b). The 5-MTHF binding did not induce a significant conformational change of SLC19A1, as the root-mean-square deviation (RMSD) between the apo- and 5-MTHF-bound structures was 1.2 Å (Fig. 2c). Though the EM densities of the glutamate moiety of 5-MTHF were unresolved in the complex structure, the assignment of the substrate was unambiguously achieved. 5-MTHF resided inside the central cavity of SLC19A1 in the perpendicular position to the cell membrane, with the pterin ring pointing to the extracellular gate (Fig. 2b).

### **Mechanism of substrate recognition by human SLC19A1**

In the structure of the SLC19A1/5-MTHF complex, the substrate-binding site was predominantly formed by TM1, 4, 7, and 10 of SLC19A1 (Fig. 2b). Notably, the electrostatic distribution of this binding site matched the charge characteristics of 5-MTHF (Fig. 2d), i.e., the polar pterin ring of 5-MTHF was wrapped in a negatively-charged pocket, and the glutamate moiety of 5-MTHF was located in a positively-charged environment.

We examined the critical residues involved in the substrate recognition of SLC19A1. On the extracellular side, the pterin ring of 5-MTHF formed hydrogen bonds with the side chains of Glu123 and Thr49 (Fig. 2e, f). At the same time, the pterin and *p*-aminobenzoyl groups of 5-MTHF

were in close contact with an array of residues through van der Waals and hydrophobic interactions, including Glu45, Ile48, Ile68, Thr69, Leu72, Tyr126, Met130, Val285, Tyr286, and His289. It is worth noting that the extra methyl group on N5 nitrogen atom of 5-MTHF could enhance the hydrophobic interactions with SLC19A1 (Fig. 2a, e, and f), thus making 5-MTHF ( $K_t$  of 1-7  $\mu\text{M}$ ) a better substrate compared to folate ( $K_t$  of  $\sim 200 \mu\text{M}$ )<sup>10</sup>. On the intracellular side, the negatively-charged glutamate moiety of 5-MTHF was accommodated by two arginine residues (Arg133 and Arg373). Additionally, Tyr281 and Gln377 also participated in polar interactions with the glutamate moiety (Fig. 2e, f). Although the overall structure of TM regions did not change between the apo- and substrate-bound SLC19A1, the side chains of several residues (Tyr126, Arg133, Tyr282, and Arg373) had detectable movements upon 5-MTHF binding. Among them, the conformational shift of Arg133 was most significant, i.e., the guanidine group of Arg133 was re-orientated to engage the substrate in the SLC19A1/5-MTHF complex (Fig. 2g and Extended Data Fig. 3b).

To verify the functional relevance of those residues involved in the substrate binding of SLC19A1, we mutated them individually and tested their effects on the transport activity in HEK293F cells (Fig. 2h and Extended Data Fig. 1b). Substitutions of Glu123, Arg133, Tyr281, and Arg373 with alanine abolished the transport activity of SLC19A1, consistent with their participation in the polar or electrostatic interactions with 5-MTHF. In comparison, the Q377A mutation only reduced the transport activity by  $\sim 40\%$ , indicating that its polar interaction with 5-MTHF was less critical than that of the four residues above. In addition, T49A, I68A, T69A, L72A, Y126A, V285A, Y286A, or H289A mutation attenuated the transport activity by 20~50%, suggesting that their hydrophobic stacking with the pterin or *p*-aminobenzoyl ring would also contribute to substrate binding. Of importance, these key residues of SLC19A1 involved in the

substrate recognition are mostly conserved among different species (Extended Data Fig. 5). In contrast, Ile48 and Met130 had minor roles as their mutations barely affect the function of SLC19A1. Intriguingly, mutation of Glu45 to alanine enhanced the transport activity by ~70%. This E45A mutation might better stabilize the unique loop structure of TM1 around the substrate-binding site (Extended Data Fig. 3c). In support of this notion, mutations of the residues adjacent to Glu45, e.g., G44R and S46I, have been identified in antifolate-drug resistant leukemia cells<sup>33,34</sup>.

SLC19 subfamily contains three members, i.e., SLC19A1, SLC19A2, and SLC19A3. Although sharing over 40% sequence identity, they engage different substrates, i.e., SLC19A1 transports folate, whereas SLC19A2 and SLC19A3 transport thiamine (vitamin B<sub>1</sub>)<sup>10</sup>. We investigated the mechanism designating the folate specificity of SLC19A1. By primary and ternary structural alignments, five out of the twelve residues of SLC19A1 comprising the binding site around the pterin and *p*-aminobenzoyl groups of 5-MTHF are not conserved in SLC19A2 and SLC19A3, i.e., Thr69, Leu72, Met130, Tyr286, and His289 (Fig. 3a-c). However, mutations of these residues to their cognates in SLC19A2 or SLC19A3 only slightly affected the transport activity of SLC19A1 (Fig. 3d and Extended Data Fig. 1c). We thus focused on the residues of SLC19A1 accommodating the negatively-charged glutamate moiety of 5-MTHF, i.e., Arg133, Tyr281, Arg373, and Gln377. While Tyr281 and Arg373 are conserved in SLC19A2 and SLC19A3, Arg133 and Gln377 become glutamate and methionine residues in SLC19A2 (Glu138 and Met401) and SLC19A3 (Glu120 and Met384), respectively (Fig. 3a-c). Replacing either of these two residues with their cognates in SLC19A2 and SLC19A3 (R133E or Q377M) completely abolished the function of SLC19A1 (Fig. 3d and Extended Data Fig. 1c). In addition, substituting the alanine residue adjacent to Arg133 to proline, i.e., A132P, caused the malfunction of SLC19A1<sup>35,36</sup>, elucidating the geometry restriction at Arg133. These results have suggested that



these two variant residues among SLC19 subfamily members would be sufficient to determine the substrate specificity, with the negatively-charged glutamate and hydrophobic methionine residues of SLC19A2 and SLC19A3 precluding folate via the electrostatic or nonpolar repulsion on its glutamate moiety.

### **TPP is the favorite coupled substrate of SLC19A1**

Although SLC19A2 and SLC19A3 both transport thiamine but not folate, most of the residues that comprise the substrate-binding pocket of SLC19A1, particularly those surrounding the pterin and *p*-aminobenzoyl groups of 5-MTHF, are highly conserved in SLC19A2 and SLC19A3 (Fig. 3a). Also, the non-conserved residues appeared to have a minor role in the transport function of SLC19A1 (Fig. 3d). These observations raised a tempting possibility that SLC19A1 might recognize specific types of thiamine derivatives as its substrate. Notably, SLC19A1 functions as an antiporter, i.e., coupling folate intake with the transport of another substrate in the opposite direction. In fact, a variety of organic phosphate anions were reported to be such coupled substrates of SLC19A1, including TPP, ATP (adenosine triphosphate), ADP (adenosine diphosphate), AMP (adenosine monophosphate), G6P (glucose 6-phosphate), and NAD<sup>+</sup> (nicotinamide adenine dinucleotide)<sup>23,37,38</sup>. It thus came to our attention that the majority of thiamine would be metabolized in cells to its active form, the organic-phosphate derivative TPP (Fig. 4a), which is the coenzyme involved in biochemical reactions of decarboxylation<sup>39</sup>.

We then pursued the cryo-EM structure of the SLC19A1/TPP complex to 3.7-Å resolution (Extended Data Fig. 6 and Table 1). Strikingly, TPP could be clearly detected in the same substrate-binding site as in the SLC19A1/5-MTHF structure (Fig. 4b, c). There was no significant conformational difference between the TPP-bound and 5-MTHF-bound SLC19A1, as the RMSD

of the two structures was 1.3 Å (Fig. 4d). TPP interacted with SLC19A1 in a manner highly reminiscent of that in 5-MTHF (Fig. 4e, f). On the extracellular side, the pyrimidine ring of TPP formed hydrogen bonds with the side chain of Glu123 and the main-chain carboxyl of Tyr286. In addition, the pyrimidine and thiazolium rings of TPP were stabilized through van der Waals and hydrophobic interactions by the similar collection of residues that interacted with the pterin and *p*-aminobenzoyl groups of 5-MTHF as described above. On the intracellular side, the negatively-charged pyrophosphate moiety of TPP was clamped by the same positively-charged Arg133 and Arg373, as well as the polar interaction with the hydroxyl of Tyr281. Notably, the side chain of Arg133 assumed the unique conformation for a better adaption of TPP (Fig. 4g and Extended Data Fig. 3b).

To validate TPP as an authentic substrate of SLC19A1, we tested its ability to compete with the uptake of [<sup>3</sup>H]-MTX. As the positive control, 5-MTHF, folate, and MTX all effectively blocked the SLC19A1-mediated intake of [<sup>3</sup>H]-MTX at 200 μM concentration. Importantly, TPP exhibited a comparable inhibitory effect with IC<sub>50</sub> of 19 μM (Fig. 4h, i). In contrast, ATP, ADP, AMP, G6P, and NAD<sup>+</sup> showed much weaker or no effect on the [<sup>3</sup>H]-MTX transport (Fig. 4h). In parallel, we measured the thermostability of SLC19A1 in the presence of different compounds (Fig. 4j). As expected, the well-documented substrates 5-MTHF and folate significantly enhanced the thermostability of SLC19A1. Among the examined organic phosphate compounds, only TPP could elevate the thermostability of SLC19A1. These results have supported that TPP is the favorite coupled substrate of SLC19A1.

## Discussion

SLC19A1 is the first identified folate transporter ubiquitously expressed in tissues and responsible for folate uptake in most types of mammalian cells<sup>9</sup>. Its action is coupled with the counter-transport of organic phosphate anions<sup>40</sup>. Although multiple cellular metabolites such as ATP, ADP, AMP, and NAD<sup>+</sup> have been documented as the coupled substrates of SLC19A1, we showed with the structural and functional analyses that TPP would be the favorite compared to those commonly recognized ones. According to the alternative access mechanism, SLC19A1 would cycle between the inward-facing and outward-facing conformations to carry its substrates across the cell membrane<sup>41</sup>. In our current structures, the extracellular (5-MTHF) and intracellular (TPP) substrates are bound to the identical site in SLC19A1, similar to that observed in some other antiporters<sup>42,43</sup>. It is plausible that cytosolic TPP could liberate 5-MTHF from the inward-facing SLC19A1 through competition under physiological conditions, and SLC19A1 would then adopt the outward-facing conformation for releasing TPP and binding extracellular 5-MTHF again (Fig. 5). The complete documentation of such a transport mechanism awaits the future structure of outward-facing SLC19A1. Folate and TPP are the coenzymes generally characterized for anabolism and catabolism, respectively. Therefore, the coordinated exchange of these two molecules by SLC19A1 might represent a novel, intrinsic part of cell metabolic regulation.

Thiamine monophosphate (TMP) might bind to SLC19A1 as a coupled substrate. Indeed, TMP effectively competed with [<sup>3</sup>H]-MTX in the transporter assay and enhanced the thermostability of SLC19A1 (Fig. 4h, j). However, given that TMP is an intermediate of thiamine metabolism and its intracellular concentration is approximately one to two orders of magnitude lower than TPP<sup>44,45</sup>, it would likely have a limited role in facilitating folate transport. On the other hand, though additional organic-phosphate anionic molecules ZMP (or AICAR, 5-aminoimidazole 4-carboxamide ribonucleoside) and cGAMP (2'3'-cyclic-GMP-AMP) were reported as the

potential substrates of SLC19A1<sup>46-49</sup>, we were unable to obtain their complex structures with SLC19A1 under the same condition as 5-MTHF and TPP (data not shown). Therefore, how SLC19A1 would recognize these molecules warrants more detailed investigations.

SLC46A1 and FRs are often specifically expressed or upregulated in cancer cells<sup>50,51</sup>. Of importance, the folate-binding sites of these two proteins are distinct from that of SLC19A1 reported here (Extended Data. Fig. 7). Such structural divergence would enable the development of new antifolate drugs that distinguish the different transport systems, thus minimizing potential adverse effects of cancer chemotherapy on normal non-malignant cells. This work has thus bridged a gap in the knowledge of the molecular mechanism of folate transport and could have broad implications for basic biology and translational research.

## References

1. Bailey, L.B. et al. Biomarkers of Nutrition for Development-Folate Review. *J. Nutr.* **145**, 1636S-1680S (2015).
2. Alam, C., Kondo, M., O'Connor, D.L. & Bendayan, R. Clinical Implications of Folate Transport in the Central Nervous System. *Trends Pharmacol. Sci.* **41**, 349-361 (2020).
3. Coppede, F. The genetics of folate metabolism and maternal risk of birth of a child with Down syndrome and associated congenital heart defects. *Front. Genet.* **6**, 223 (2015).
4. Qiu, A. et al. Identification of an intestinal folate transporter and the molecular basis for hereditary folate malabsorption. *Cell* **127**, 917-28 (2006).
5. Henderson, G.B. Folate-binding proteins. *Annu. Rev. Nutr.* **10**, 319-35 (1990).
6. Kelemen, L.E. The role of folate receptor alpha in cancer development, progression and treatment: cause, consequence or innocent bystander? *Int. J. Cancer* **119**, 243-50 (2006).
7. Kamen, B.A., Wang, M.T., Streckfuss, A.J., Peryea, X. & Anderson, R.G. Delivery of folates to the cytoplasm of MA104 cells is mediated by a surface membrane receptor that recycles. *J. Biol. Chem.* **263**, 13602-9 (1988).
8. Dixon, K.H., Lanpher, B.C., Chiu, J., Kelley, K. & Cowan, K.H. A novel cDNA restores reduced folate carrier activity and methotrexate sensitivity to transport deficient cells. *J. Biol. Chem.* **269**, 17-20 (1994).
9. Goldman, I.D., Lichtenstein, N.S. & Oliverio, V.T. Carrier-mediated transport of the folic acid analogue, methotrexate, in the L1210 leukemia cell. *J. Biol. Chem.* **243**, 5007-17 (1968).
10. Zhao, R. & Goldman, I.D. Folate and thiamine transporters mediated by facilitative carriers (SLC19A1-3 and SLC46A1) and folate receptors. *Mol. Aspects Med.* **34**, 373-85 (2013).
11. Matherly, L.H., Wilson, M.R. & Hou, Z. The major facilitative folate transporters solute carrier 19A1 and solute carrier 46A1: biology and role in antifolate chemotherapy of cancer. *Drug Metab. Dispos.* **42**, 632-49 (2014).
12. Rothberg, K.G., Ying, Y.S., Kolhouse, J.F., Kamen, B.A. & Anderson, R.G. The glycopospholipid-linked folate receptor internalizes folate without entering the clathrin-coated pit endocytic pathway. *J. Cell Biol.* **110**, 637-49 (1990).
13. Zhao, R., Matherly, L.H. & Goldman, I.D. Membrane transporters and folate homeostasis: intestinal absorption and transport into systemic compartments and tissues. *Expert Rev. Mol. Med.* **11**, e4 (2009).
14. Matherly, L.H., Hou, Z. & Deng, Y. Human reduced folate carrier: translation of basic biology to cancer etiology and therapy. *Cancer Metastasis Rev.* **26**, 111-28 (2007).
15. Gonen, N. & Assaraf, Y.G. Antifolates in cancer therapy: structure, activity and mechanisms of drug resistance. *Drug Resist. Updat.* **15**, 183-210 (2012).
16. Zhao, R. & Goldman, I.D. Resistance to antifolates. *Oncogene* **22**, 7431-57 (2003).
17. Parker, J.L. et al. Structural basis of antifolate recognition and transport by PCFT. *Nature* **595**, 130-134 (2021).
18. Chen, C. et al. Structural basis for molecular recognition of folic acid by folate receptors. *Nature* **500**, 486-9 (2013).
19. Wibowo, A.S. et al. Structures of human folate receptors reveal biological trafficking states and diversity in folate and antifolate recognition. *Proc. Natl. Acad. Sci. USA* **110**, 15180-8 (2013).

20. Tsutsumi, N. et al. Structure of human Frizzled5 by fiducial-assisted cryo-EM supports a heterodimeric mechanism of canonical Wnt signaling. *Elife* **9**(2020).
21. Mukherjee, S. et al. Synthetic antibodies against BRIL as universal fiducial marks for single-particle cryoEM structure determination of membrane proteins. *Nat. Commun.* **11**, 1598 (2020).
22. Ereno-Orbea, J. et al. Structural Basis of Enhanced Crystallizability Induced by a Molecular Chaperone for Antibody Antigen-Binding Fragments. *J. Mol. Biol.* **430**, 322-336 (2018).
23. Goldman, I.D. The characteristics of the membrane transport of amethopterin and the naturally occurring folates. *Ann. N. Y. Acad. Sci.* **186**, 400-22 (1971).
24. Yan, N. Structural Biology of the Major Facilitator Superfamily Transporters. *Annu. Rev. Biophys.* **44**, 257-83 (2015).
25. Bai, X., Moraes, T.F. & Reithmeier, R.A.F. Structural biology of solute carrier (SLC) membrane transport proteins. *Mol. Membr. Biol.* **34**, 1-32 (2017).
26. Doyle, D.A. et al. The structure of the potassium channel: molecular basis of K<sup>+</sup> conduction and selectivity. *Science* **280**, 69-77 (1998).
27. Dutzler, R., Campbell, E.B., Cadene, M., Chait, B.T. & MacKinnon, R. X-ray structure of a ClC chloride channel at 3.0 Å reveals the molecular basis of anion selectivity. *Nature* **415**, 287-94 (2002).
28. Feng, L., Campbell, E.B., Hsiung, Y. & MacKinnon, R. Structure of a eukaryotic ClC transporter defines an intermediate state in the transport cycle. *Science* **330**, 635-41 (2010).
29. Zhang, Z. & Chen, J. Atomic Structure of the Cystic Fibrosis Transmembrane Conductance Regulator. *Cell* **167**, 1586-1597 e9 (2016).
30. Screpanti, E. & Hunte, C. Discontinuous membrane helices in transport proteins and their correlation with function. *J. Struct. Biol.* **159**, 261-7 (2007).
31. McMahon, C. et al. Yeast surface display platform for rapid discovery of conformationally selective nanobodies. *Nat. Struct. Mol. Biol.* **25**, 289-296 (2018).
32. Wu, X. & Rapoport, T.A. Cryo-EM structure determination of small proteins by nanobody-binding scaffolds (Legobodies). *Proc. Natl. Acad. Sci. USA* **118**(2021).
33. Wong, S.C. et al. Impaired membrane transport in methotrexate-resistant CCRF-CEM cells involves early translation termination and increased turnover of a mutant reduced folate carrier. *J. Biol. Chem.* **274**, 10388-94 (1999).
34. Drori, S., Jansen, G., Mauritz, R., Peters, G.J. & Assaraf, Y.G. Clustering of mutations in the first transmembrane domain of the human reduced folate carrier in GW1843U89-resistant leukemia cells with impaired antifolate transport and augmented folate uptake. *J. Biol. Chem.* **275**, 30855-63 (2000).
35. Schuetz, J.D. et al. Membrane protein changes in an L1210 leukemia cell line with a translocation defect in the methotrexate-tetrahydrofolate cofactor transport carrier. *J. Biol. Chem.* **264**, 16261-7 (1989).
36. Brigle, K.E., Spinella, M.J., Sierra, E.E. & Goldman, I.D. Characterization of a mutation in the reduced folate carrier in a transport defective L1210 murine leukemia cell line. *J. Biol. Chem.* **270**, 22974-9 (1995).
37. Henderson, G.B. & Zevely, E.M. Structural requirements for anion substrates of the methotrexate transport system in L1210 cells. *Arch. Biochem. Biophys.* **221**, 438-46 (1983).
38. Zhao, R. et al. Impact of the reduced folate carrier on the accumulation of active thiamin metabolites in murine leukemia cells. *J. Biol. Chem.* **276**, 1114-8 (2001).

39. Lonsdale, D. A review of the biochemistry, metabolism and clinical benefits of thiamin(e) and its derivatives. *Evid. Based Complement Alternat. Med.* **3**, 49-59 (2006).
40. Hou, Z. & Matherly, L.H. Biology of the major facilitative folate transporters SLC19A1 and SLC46A1. *Curr. Top. Membr.* **73**, 175-204 (2014).
41. Jardetzky, O. Simple allosteric model for membrane pumps. *Nature* **211**, 969-70 (1966).
42. Huang, Y., Lemieux, M.J., Song, J., Auer, M. & Wang, D.N. Structure and mechanism of the glycerol-3-phosphate transporter from *Escherichia coli*. *Science* **301**, 616-20 (2003).
43. Fluman, N., Ryan, C.M., Whitelegge, J.P. & Bibi, E. Dissection of mechanistic principles of a secondary multidrug efflux protein. *Mol. Cell* **47**, 777-87 (2012).
44. Tallaksen, C.M., Bohmer, T., Bell, H. & Karlsen, J. Concomitant determination of thiamin and its phosphate esters in human blood and serum by high-performance liquid chromatography. *J. Chromatogr.* **564**, 127-36 (1991).
45. Tallaksen, C.M., Bohmer, T., Karlsen, J. & Bell, H. Determination of thiamin and its phosphate esters in human blood, plasma, and urine. *Methods Enzymol.* **279**, 67-74 (1997).
46. Zhao, R., Gao, F. & Goldman, I.D. Reduced folate carrier transports thiamine monophosphate: an alternative route for thiamine delivery into mammalian cells. *Am. J. Physiol. Cell Physiol.* **282**, C1512-7 (2002).
47. Luteijn, R.D. et al. SLC19A1 transports immunoreactive cyclic dinucleotides. *Nature* **573**, 434-438 (2019).
48. Ritchie, C., Cordova, A.F., Hess, G.T., Bassik, M.C. & Li, L. SLC19A1 Is an Importer of the Immunotransmitter cGAMP. *Mol. Cell* **75**, 372-381 e5 (2019).
49. Visentin, M., Zhao, R. & Goldman, I.D. Augmentation of reduced folate carrier-mediated folate/antifolate transport through an antiport mechanism with 5-aminoimidazole-4-carboxamide riboside monophosphate. *Mol. Pharmacol.* **82**, 209-16 (2012).
50. Matherly, L.H., Hou, Z. & Gangjee, A. The promise and challenges of exploiting the proton-coupled folate transporter for selective therapeutic targeting of cancer. *Cancer Chemother. Pharmacol.* **81**, 1-15 (2018).
51. Assaraf, Y.G., Leamon, C.P. & Reddy, J.A. The folate receptor as a rational therapeutic target for personalized cancer treatment. *Drug Resist. Updat.* **17**, 89-95 (2014).

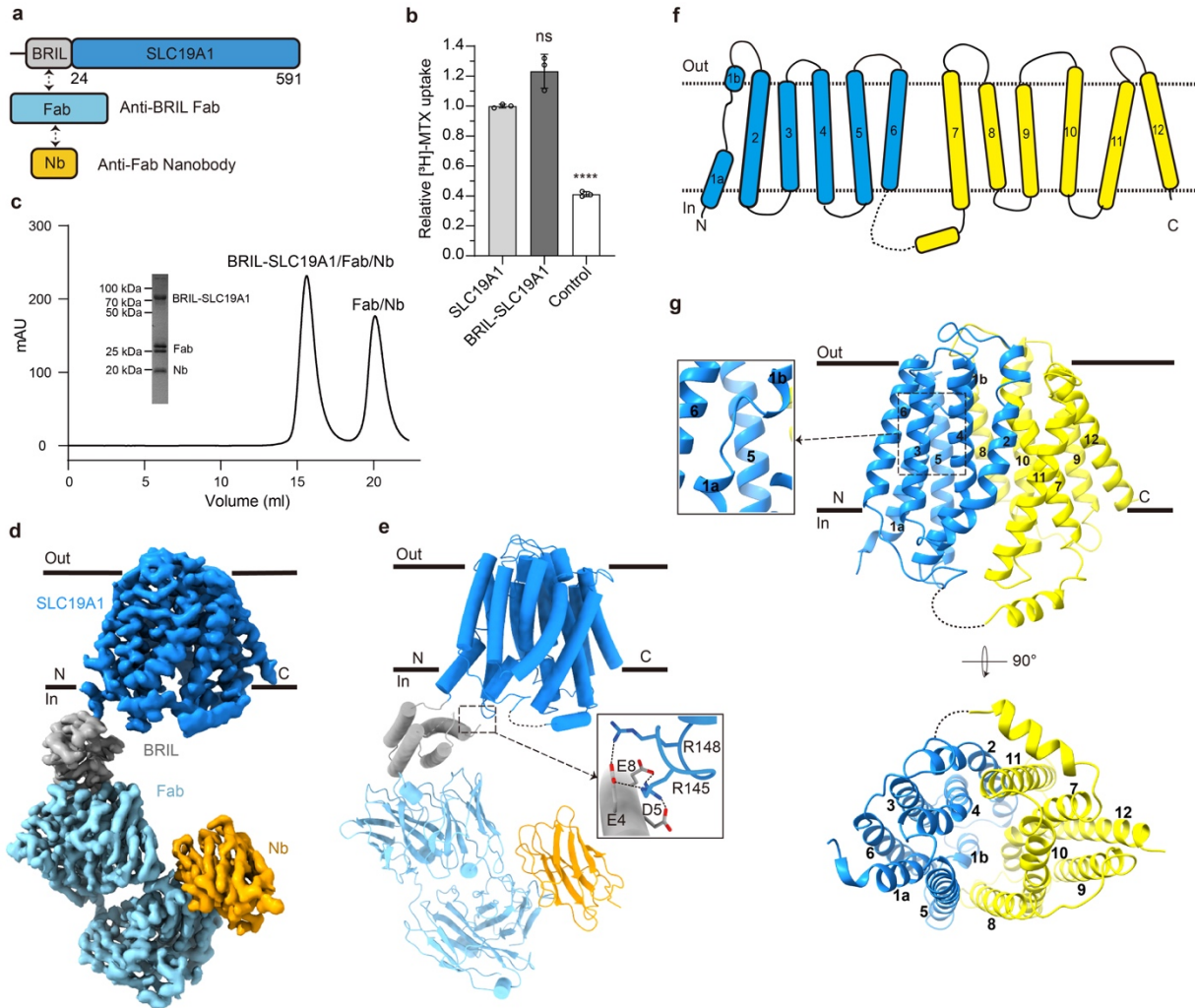


**Fig. 1 | Cryo-EM structure of the BRIL-SLC19A1/Fab/Nb complex.**

**a**, Schematic diagrams of BRIL-SLC19A1, anti-BRIL Fab, and anti-Fab Nanobody. **b**,  $[^3\text{H}]\text{-MTX}$  uptake assay to verify the function of BRIL-SLC19A1. The results are normalized to the activity of wild-type SLC19A1. All experiments were done in triplicates. ( $n = 3$ , mean  $\pm$  s.d.). ns, non-significant; \*\*\*\*  $P < 0.0001$  (T-test). **c**, Profile of size exclusion chromatography (SEC) for the complex purification and the SDS-PAGE results to show the protein purity. **d**, Cryo-EM map of the BRIL-SLC19A1/Fab/Nb complex. **e**, Overall structure of the BRIL-SLC19A1/Fab/Nb complex.  $\alpha$ -helices are shown in cylinders and  $\beta$ -strands are in ribbon. The residues of BRIL and SLC19A1 that are involved in electrostatic interactions are shown with side chains. **f**, Cartoon



diagram for the transmembrane (TM) domain of SLC19A1. The TM numbers are labeled, and the plasma membrane is indicated with dotted lines. **g**, Ribbon presentation of the SLC19A1 structure in two views. Two half TM bundles are colored in blue (TM1-6) and yellow (TM7-12), respectively. A close-up view of the unwound region of TM1 is shown in an inset.

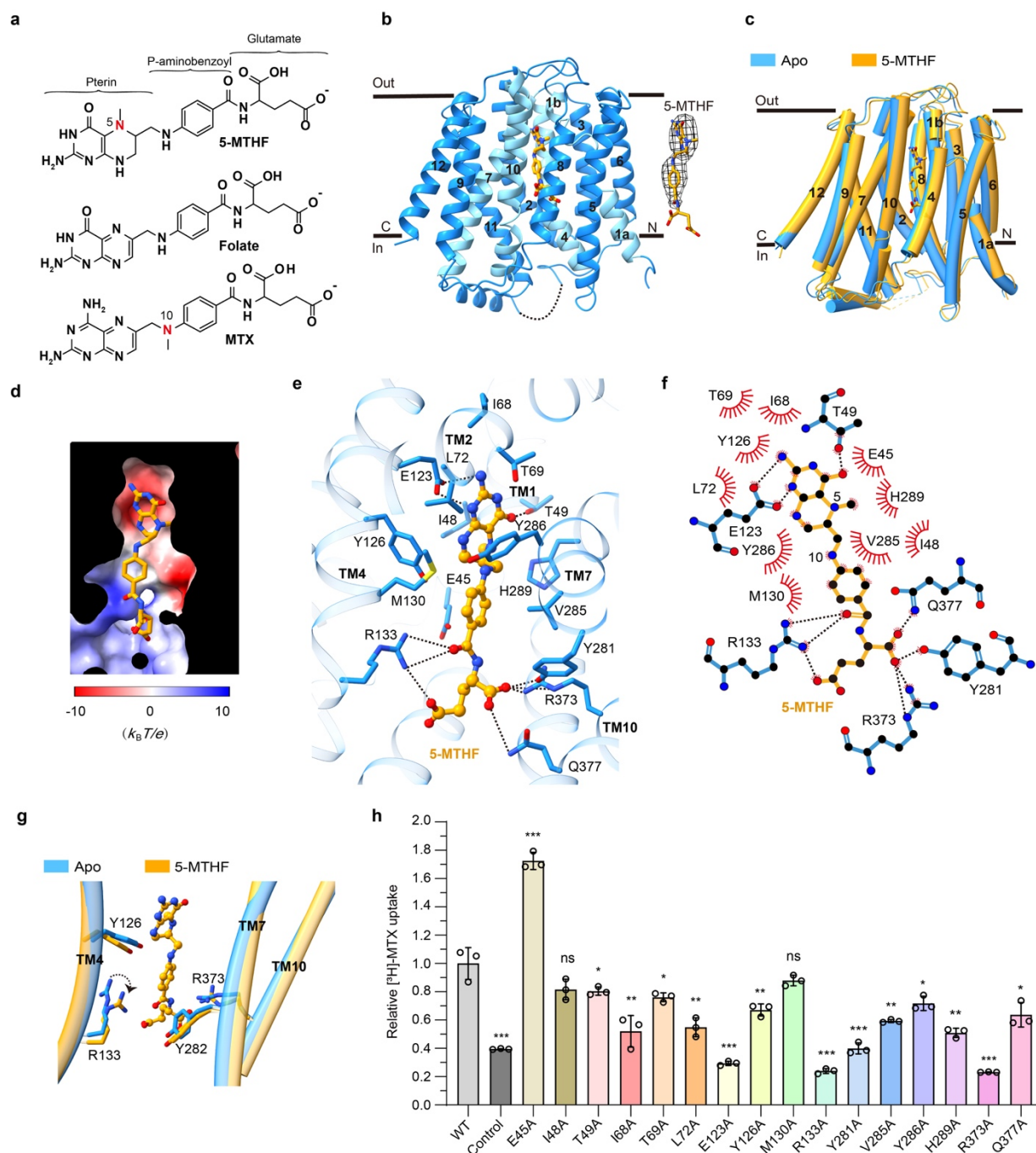


**Fig. 2 | Cryo-EM structure of the SLC19A1/5-MTHF complex.**

**a**, Chemical structures of several folate analogs, including 5-MTHF (5-methyltetrahydrofolate), folate, and MTX (methotrexate). The constituent moieties of 5-MTHF are indicated. **b**, Ribbon diagram of SLC19A1 in complex with 5-MTHF. The four TMs (TM1, 4, 7, and 10) interacting with 5-MTHF are colored in cyan and the other ones are colored in blue. 5-MTHF is shown in

sticks and its cryo-EM densities are shown in black meshes. **c**, Superposition of the apo and 5-MTHF-bound SLC19A1 structures. **d**, The electrostatic potential (in units of  $k_B T/e$ , where  $k_B$  is the Boltzmann constant,  $T$  is the absolute temperature and  $e$  is the elementary charge) of the substrate-binding pocket in SLC19A1, as calculated at pH 7.0 and 0.15 M concentrations of monovalent cations and anions. 5-MTHF is shown in sticks. **e**, Ribbon presentation of the substrate-binding site in SLC19A1. The residues participating in 5-MTHF binding are indicated with side chains ( $< 4.0 \text{ \AA}$ ). Hydrogen bonds and salt bridges are depicted as dashed lines. **f**, A schematic summary of the interactions between SLC19A1 and 5-MTHF. **g**, Overlay of the substrate-binding regions in the apo and 5-MTHF-bound SLC19A1 structures. The residues with obvious conformational changes are shown with side chains. **h**, The [ $^3\text{H}$ ]-MTX uptake activities of SLC19A1 mutants. The results are normalized to the activity of wild-type SLC19A1. All experiments were done in triplicates ( $n = 3$ , mean  $\pm$  s.d.). ns, non-significant; \*  $P < 0.01$ ; \*\*  $P < 0.005$ ; \*\*\*  $P < 0.001$  (T-test).

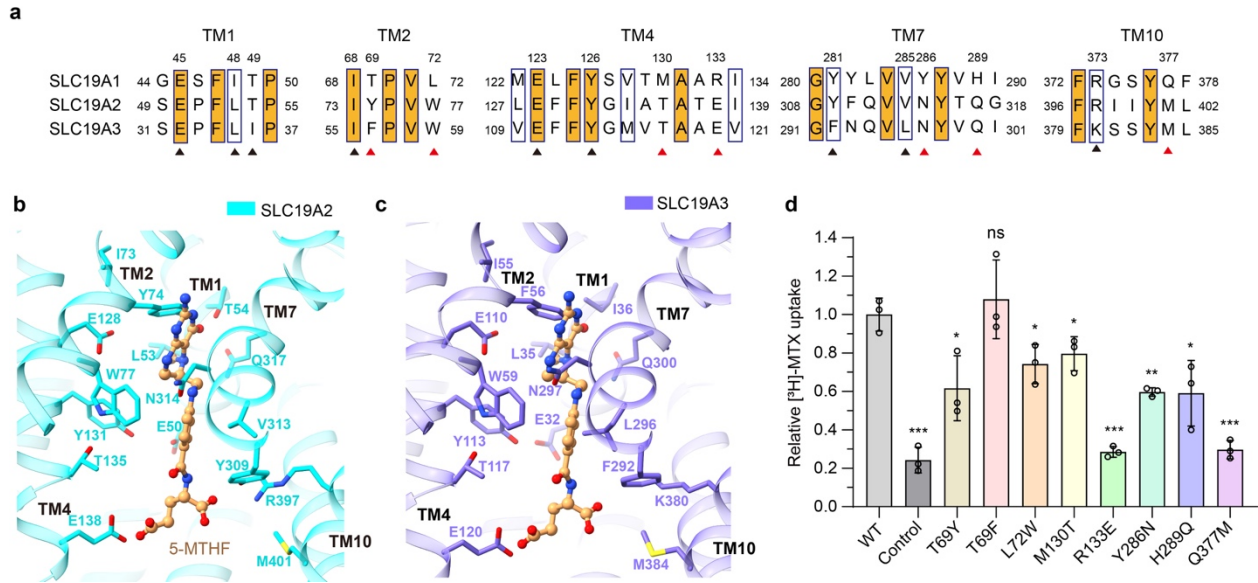


**Fig. 3 | Analyses of the substrate discrimination mechanism of SLC19 subfamily members.**

**a**, Sequence alignment of the three SLC19 family members. The partially conserved residues are indicated with blue boxes and the strictly conserved ones are further filled with orange color. The residues of SLC19A1 that involved in 5-MTHF binding are indicated. The conserved and non-conserved ones are denoted by black and red arrowheads, respectively. **b-c**, Ribbon presentation of the 5-MTHF binding site in SLC19A2 and SLC19A3. The structures of SLC19A2 and SLC19A3 are predicted by AlphaFold. 5-MTHF is modeled into these structures based on the superposition with our SLC19A1/5-MTHF structure. The cognates of SLC19A2 and SLC19A3 corresponding to the 5-MTHF interaction residues of SLC19A1 are indicated. **d**, Functional verification of the non-conserved residues for SLC19A1 using the [<sup>3</sup>H]-MTX uptake assay. The results are normalized to the activity of wild-type SLC19A1. All experiments were done in triplicates (n = 3, mean ± s.d.). ns, non-significant; \* P < 0.01; \*\* P < 0.005; \*\*\* P < 0.001 (T-test).

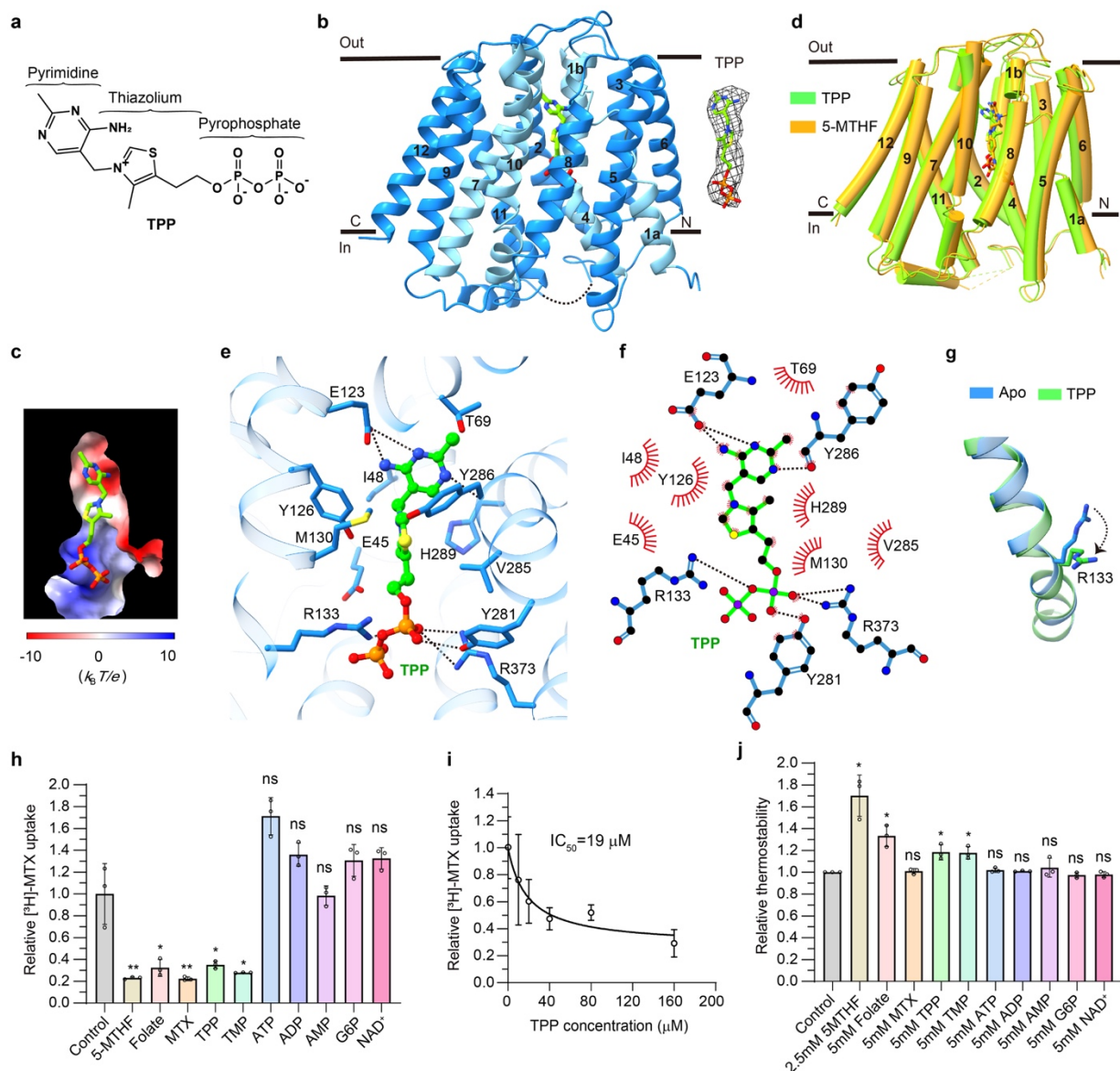


**Fig. 4 | Verification of TPP as the favorite coupled substrate of SLC19A1.**

**a**, The chemical structure of TPP. The constituent moieties are indicated. **b**, Ribbon diagram of SLC19A1 in complex with TPP, TPP is shown in sticks and its cryo-EM densities are shown in black meshes. **c**, The electrostatic potential of the TPP binding site. **d**, Structural comparison of the TPP- and 5-MTHF-bound SLC19A1. **e**, Ribbon presentation of the TPP-binding site in SLC19A1. The residues involved in the interaction with TPP are shown with side chains. **f**, A schematic summary of the interactions between SLC19A1 and TPP. **g**, Conformational change of

the side chain of Arg133 between apo and TPP-bound SLC19A1 structures. **h**, Inhibitory effect of different compounds on the [<sup>3</sup>H]-MTX uptake activity of SLC19A1. All the molecules were tested at the concentration of 200  $\mu$ M. The results are normalized to the activity of the control experiment in which no inhibitors are added. All experiments were done in triplicates ( $n = 3$ , mean  $\pm$  s.d.). ns, non-significant; \*  $P < 0.01$ ; \*\*  $P < 0.005$  (T-test). **i**, Quantitative measurement of the potency of TPP in inhibiting the [<sup>3</sup>H]-MTX delivery by SLC19A1. The results are normalized to the MTX transport activity of SLC19A1 in the absence of TPP. All experiments were done in triplicates ( $n = 3$ , mean  $\pm$  s.d.).  $IC_{50}$  was calculated by fitting to a nonlinear regression model. **j**, Quantification of the fluorescence-detection size-exclusion chromatography (FSEC)-based thermostability assay. The concentrations of molecules are indicated. The thermostability is calculated relative to the control experiment in which SLC19A1 was not incubated with any compounds. All experiments were done in triplicates ( $n = 3$ , mean  $\pm$  s.d.). ns, non-significant; \*  $P < 0.01$  (T-test).

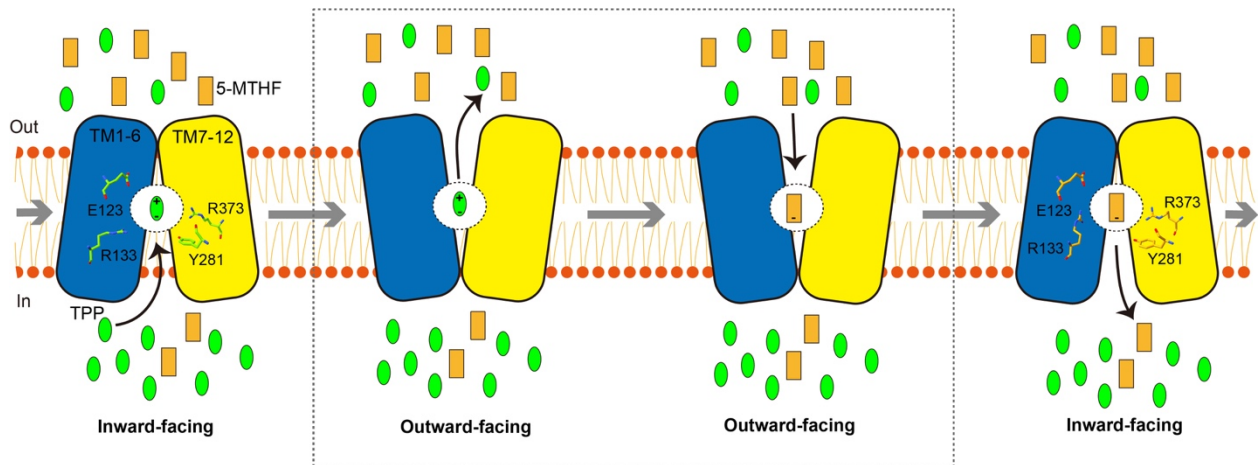


**Fig. 5 | Model of the substrate transport cycle of SLC19A1.**

SLC19A1 utilizes the alternating access mechanism to reverse transport two substrates. Under physiological conditions, 5-MTHF and TPP are likely the favorite extracellular and intracellular substrates of SLC19A1, respectively. They compete for the same binding site within the central cavity of SLC19A1. The four key residues (Glu123, Arg133, Tyr281, and Arg373) for substrate recognition are indicated.

## **Acknowledgements**

We thank the Cryo-EM platform and the School of Life Sciences of PKU for cryo-electron microscopy data collection. We are grateful to Dr. Guopeng Wang, Bo Shao, Xia Pei, and Dr. Ning Gao for their help in cryo-EM experiments. We thank Shitang Huang at the National Center for Protein Sciences of Peking University for assistance with radioactive experiments. We thank Jinkun Xu in Long Li's lab for assistance with the nanobody screening. We thank Qing Chang and Wenqi Li at Beijing Advanced Innovation Center for Structural Biology of Tsinghua University for assistance with our pilot experiments to verify the protein-small molecule interactions.

**Funding:** This research was funded by the National Key Research and Development Program of China (to Z.Z., NO. 2021YFA1302300) and the National Natural Science Foundation of China (to Z.Z., NO. 32171201). The study was also supported by Center for Life Sciences (CLS), School of Life Sciences (SLS) of Peking University, the SLS-Qidong innovation fund, Li Ge-Zhao Ning Life Science Youth Research Foundation, and the State Key Laboratory of Membrane Biology of China.

**Author contributions:** Y.D., X.D., and H.Z. did the cloning and protein purification. X.D. screened nanobodies against SLC19A1. Y.D., C.Q., and Z.G. collected the cryo-EM data. Y.D. and Z.Z. processed the EM data. Z.Z. built and refined the structural models. Y.D. and D.Z. performed the MTX uptake experiments. Y.D. carried out the thermostability assay. C.-H.L. assisted in model building and structural analysis. Z.Z. wrote the manuscript with input and support from all co-authors. J.Y. revised the manuscript.

**Competing interests:** The authors declare no competing interests.



### **Data availability**

Cryo-EM density maps of the apo, 5-MTHF-bound, and TPP-bound SLC19A1 have been deposited in the Electron Microscopy Data Bank under the accession codes EMD-xxxxx, EMD-xxxxx, and EMD-xxxxx. Their atomic coordinates have been deposited in the Protein Data Bank under accession codes XXXX, XXXX, and XXXX.